COMPUTATIONAL STUDY FOR HIGH-LIFT AERODYNAMICS RESEARCH IN JAXA

Mitsuhiro MURAYAMA, Yuzuru YOKOKAWA, Hiroyuki KATO, Kanazaki MASAHIRO, Kazuomi YAMAMOTO, and Takeshi ITO
Japan Aerospace Exploration Agency

Keywords: *High-Lift, CFD*

Abstract

In Civil Transport Team of Japan Aerospace Exploration Agency, researches to develop design technologies for advanced high-lift devices in the aerodynamics and aeroacoustics have been conducted combining CFD and wind tunnel testing. A series of wind tunnel testing using a realistic civil aircraft high-lift model have been conducted from 2005 to 2008. In this paper, several computational studies related to the wind tunnel tests for high-lift aerodynamics are presented. Influence of the boundary layer transition with a transition prediction method based on e^N method and semi-empirical approaches is evaluated. The influence of brackets to support the high-lift devices is also discussed and interference of disturbed wakes by the supports to the flows is shown. CFD investigation of wind tunnel wall interferences using half-span testing model shows the influence of the boundary layer spacer to the flow and the best height of the spacer. Investigations of the interferences between the nacelle-pylon and high-lift devices with nacelle-chine effect and setting effect of high-lift devices and their CFD predictions are also shown. The capability and research areas required for further efforts are discussed.

1 Introduction

Improvement of the aerodynamic performance for take-off and landing can produce large benefits on payload and fuel consumption [1-2]. Efficient high-lift devices with simplified structure largely contribute to reduce the weight, production cost, and maintenance cost. Due to the recent demand in the environmental problems around airports, successful design to reduce the aeroacoustic noise from the high-lift devices while keeping the aerodynamic performance has been also required for the reduction of the airframe noise.

With the recent development of CFD technologies, optimization algorithms, and computational environments, CFD is expected to play an important role to improve the performance and develop the advanced high-lift devices. However, multi-element high-lift wing system that utilizes leading-edge slats and trailing-edge flaps complicates the flow features due to the laminar-turbulent transition of the boundary layer, flow separation, interaction of wakes of each element, and so on. For a realistic high-lift configuration with engine-nacelle-pylon mounted under the wing, the stall phenomena are often largely affected by the complex flow interaction between the nacelle-pylon and the high-lift devices. Precise prediction of the aerodynamic forces such as maximum lift (C_{Lmax}), lift to drag ratio (L/D), and Reynolds number (Re) effects for the three-dimensional high-lift configurations is still a challenging task. Physical understanding of the dominant aerodynamic phenomena and efforts to improve CFD for such complicated flows around realistic high-lift configurations are required in conjunction with experiments to improve the performance. In European EUROLIFT project [3-5], developments of aerodynamic analysis for high-lift system have been intensively conducted in conjunction with experiments.

In Civil Transport Team of Japan Aerospace Exploration Agency (JAXA), researches to develop design technologies for advanced high-lift devices have been conducted.

Both researches in the aerodynamics [6-22] and aeroacoustics [23-27] for the high-lift devices have been conducted in conjunction with experiments. In this paper, the CFD researches for high-lift aerodynamics are presented.

At the early researches, basic CFD validation studies have been conducted for two-dimensional airfoils and simplified three-dimensional wing-fuselage configurations [6-9]. Grid applicability and turbulence model dependency have been mainly evaluated using multi-block structured and hybrid unstructured mesh systems using several CFD codes.

As the following researches, the wind tunnel tests and CFD using a research model of more realistic aircraft high-lift configuration have been conducted in JAXA [10-23]. The model, denoted *JSM*, has the leading-edge slat, trailing-edge flaps, fuselage, nacelle-pylon, and Flap Track Fairing (FTF). A series of wind tunnel tests were conducted at $6.5m \times 5.5m$ JAXA Lowspeed Wind Tunnel in October 2005 - February 2006, March - April 2007, and November - December 2007. The fourth wind tunnel test will be conducted in August 2008.

The objectives of the wind tunnel tests are (1) to provide the detailed and systematic experimental data which can be disclosed for CFD validation, (2) to improve the measurement technologies, (3) to validate and improve design technologies, and (4) to increase physical understanding of the dominant aerodynamic phenomena of high-lift flows over a realistic aircraft configuration. In the wind tunnel tests, various kinds of data have been obtained as for the laminar-turbulent transition of the boundary layer and the roughness effects, the interferences between the nacelle-pylon and high-lift devices, the setting effects of high-lift devices using aerodynamic optimization method, the additional aerodynamic devices to improve the performance, and so on. The first CFD workshop to validate and improve CFD technologies was also conducted using the data in the domestic communities including several companies and universities in October 2006. Some of the related papers are Refs. 15, 28, and 29.

In this paper, several computational studies related to the wind tunnel tests are presented; (1) evaluation of influence of boundary layer transition and a transition prediction method, (2) influence of brackets to support the high-lift devices, (3) investigation of wind tunnel wall interferences, (4) investigation of the interferences between the nacelle-pylon and high-lift devices with nacelle-chine effect, and (5) investigation of setting effect of high-lift devices and its CFD prediction.

2 Model Geometry

Figure 1 shows the wind tunnel testing model in JAXA, *JSM*, tested at JAXA $6.5m \times 5.5m$ Low-speed Wind Tunnel (JAXA-LWT1). JAXA-LWT1 is an atmospheric pressure closed-circuit wind tunnel with an octagonal cross section. The scale of the wind tunnel testing model is roughly 1/6 of the assumed 100-passenger-class aircraft. The lengths of the wing half-span and fuselage are $2.3m$ and $4.9m$, respectively. *MAC* of this model is $0.529m$. The model has leading-edge slats supported by eight slat brackets, a double-slotted flap at inboard and a single-slotted flap at outboard with a circular fuselage, a flow-through nacelle-pylon mounted under the wing, and three FTFs. Two kinds of nacelles, a long-nacelle and a short-nacelle with core, can be attached on the model. In the wind tunnel tests, three-dimensional aerodynamic interferences between the wing and nacelle-pylon were investigated by comparison of several different configurations such as configurations with/without the nacelle-pylon, configurations with a short-type or long-type nacelle, configurations with/without the inboard slat cut-off between the fuselage and inboard slat, and so on as shown in Fig. 2.

The half-span model was employed to achieve higher *Re* in this wind tunnel testing. The model was mounted vertically on the turntable to change the angle of attack. To avoid interference between the model and the boundary layer of the bottom wind tunnel wall, a spacer with height of $150mm$ was inserted between the bottom wind tunnel wall and fuselage. Space with height of $10mm$ was opened between the spacer and fuselage and the space was filled with a labyrinth-like seal. The total height from the bottom wind tunnel wall to

the fuselage is 160*mm*. The spacer has the same shape with the fuselage symmetry plane. The symmetry plane of the fuselage is simply extended to the tunnel wall.

In the testing, various kinds of measurements were conducted to verify CFD analysis in detail [10-14, 21-23]. Five-component aerodynamic forces, surface pressure with pressure taps and Pressure Sensitive Paint (PSP) were obtained. Static surface pressures using 456 static pressure taps were measured at seven cross sections on the wing, four cross sections on the fuselage, and several points on the pylon. Figure 3 shows the locations of the cross sections for the static pressure measurement on the wing and fuselage. Surface flow visualizations were carried out with tuft, oil flow, and china clay to reveal the flow phenomena such as separation and transition. In the testing, moreover, unsteady pressure, velocity distribution around the model using Particle Image Velocimetry (PIV), Aeroacoustic noise sources using phased array microphones were also measured.

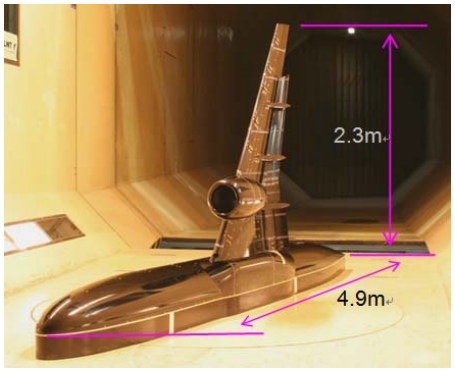

Fig. 1 Wind tunnel testing model, *JSM*, at a landing setting in JAXA-LWT1

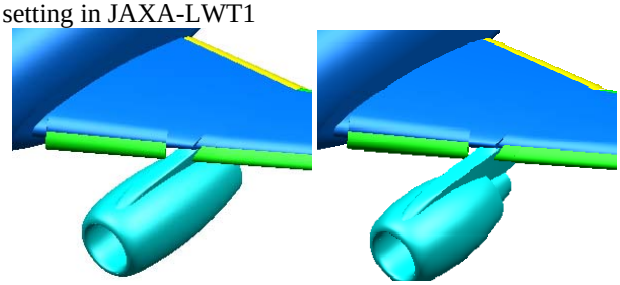

(a) Long-nacelle (b) Short-nacelle

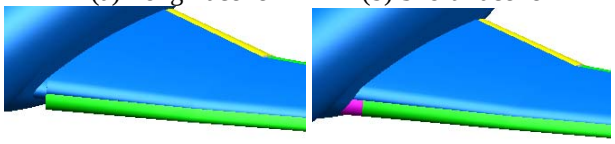

(c) Nacelle-Off (d) Continuous slat without inboard slat cut-off

Fig. 2 Configurations for wind tunnel tests

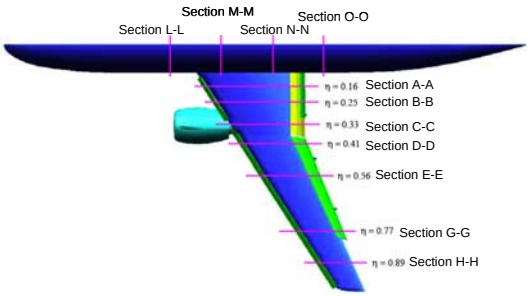

Fig. 3 Cross sections for static pressure measurement

3 Computational method and conditions

Most of the computations in this study are conducted using an unstructured mesh CFD code. As the unstructured mesh generator and flow solver, MEGG3D [30-33] and TAS code [34-35] is used in this study. MEGG3D can generate nearly-isotropic triangular surface mesh with a direct advancing front method and tetrahedral volume mesh using Delaunay or advancing front tetrahedral meshing, hybrid volume mesh composed of tetrahedrons, prisms, pyramids, and hexahedra for viscous flows.

Compressible Reynolds-averaged Navier-Stokes equations are solved on the unstructured mesh by a cell-vertex finite volume method. HLLEW method [36] is used for the numerical flux computations. The second-order spatial accuracy is realized by Unstructured MUSCL-scheme [37]. LU-SGS implicit method [38] is used for time integration. In this study, Spalart-Allmaras 1-eq turbulence model is used with a modification in the production term to decrease dissipation in the vortex core [39-40]. If some laminar regions are prescribed to simulate boundary layer transition, the term, *S*, in the production term is simply set to zero in the regions. In the specification, generation of turbulent eddy viscosity is limited in the prescribed regions, while the advection from upstream is allowed.

In this paper, computational results of the landing configurations are shown. In the computations, M_∞ is 0.175 and *Re* is 2.1×10^6 based on *MAC*. The computations were carried out on Numerical Simulator III in JAXA (Fujitsu PRIMEPOWER HPC2500) [41].

4 Results

4.1 Evaluation of influence of boundary layer transition and a transition prediction method

Aerodynamic forces at the flight *Re* condition are often extrapolated from the results at sub-scale wind tunnel *Re* conditions. C_{Lmax} is expected to increase with increasing *Re*. However, the adverse *Re* effects can occur in some cases. The change of boundary layer transition by *Re* can be one of the reasons to cause the adverse *Re* effects. The effect of the transition to the aerodynamic performance should be well estimated with the transition prediction methods.

First, the computational results assuming fully turbulent flows and flows with prescribed laminar regions are compared to investigate the sensitivity. The computational results at the configuration with the long-nacelle are compared. FTF and brackets to support the slats and aft-flap are excluded in the computations. The prescribed laminar regions are based on the experimental observations by the china-clay visualization with several simplifications as shown in Figs. 4-5.

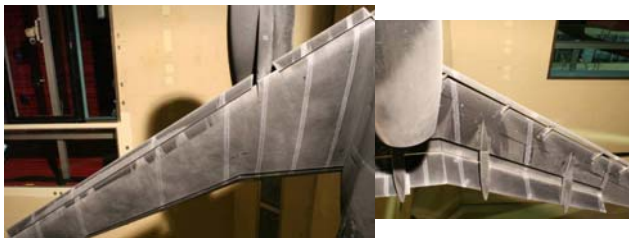

Fig. 4 China-clay visualization of boundary layer transition at $\alpha = 10°$ (Black: Laminar, White: Turbulent)

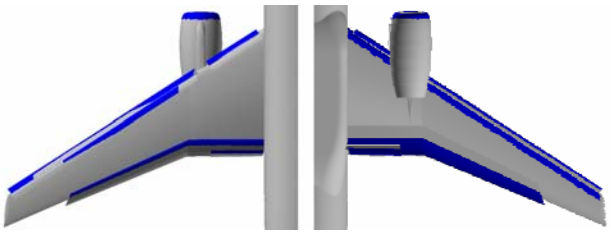

(a) Upper surface (b) Lower surface

Fig. 5 Boundary layer transition assumed in computations at $\alpha = 10°$ (Blue: Laminar, Gray: Turbulent)

Figure 6 shows C_L-α and C_L-C_D for computed results and experimental results after the correction of the wind tunnel wall. As for C_L-α, the computational results considering the boundary layer transition show higher C_L, especially at higher angles of attack, and the slope of the C_L-α shows better agreement with experimental results. While, the stall angle of attack and C_{Lmax} were slightly overestimated and the consideration of the boundary layer transition does not improve the stall prediction for the present long nacelle model. The nacelle-interference to the flows was relatively large and the boundary layer transition on the wing was not a main factor for the stall phenomena at this configuration.

As for C_L-C_D, both computational results overestimate C_D. The differences in C_D at constant C_L are about 200 cts. (1 cts. = 1×10^{-4}) at lower angles of attack and about 400 cts. at higher angles of attack and the curve of C_L-C_D is more opened in the experimental results. The computational results with specified boundary layer transition show the decrease of C_D by 40 drag counts. However, the difference with experimental results is still large.

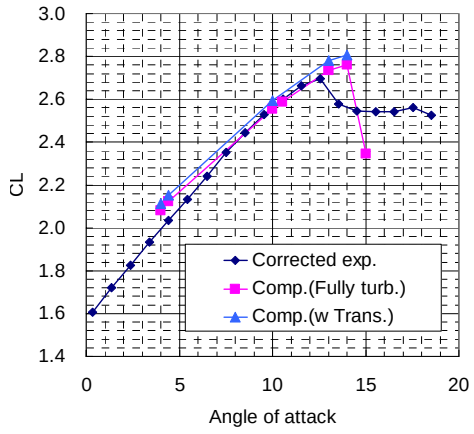

(a) C_L-α

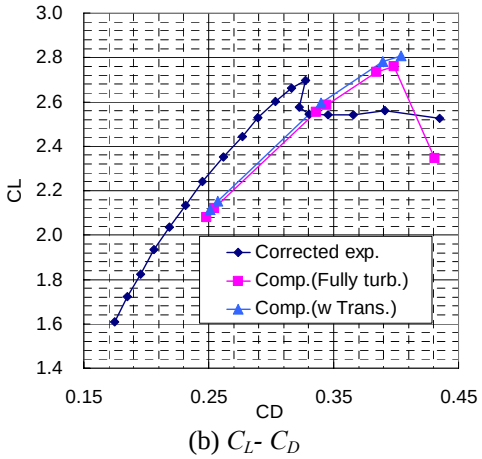

(b) C_L- C_D

Fig. 6 Comparison of aerodynamic forces with/without boundary layer transition

Figure 7 shows the comparisons of C_p at α = 10°. The results considering the specified transition flow show higher suction peaks by the acceleration of flow near the leading-edges and better agreement with experimental results especially at higher angles of attack. At Section B-B near the fuselage, however, the suction peaks of each element are lower than experimental results even in the computation considering the specified transition flow.

In this section, the sensitivity of the boundary layer transition on the aerodynamic forces has been shown. The differences between the experimental and computational results in C_D and C_p for the suction peaks near the fuselage are discussed later section with CFD considering the wind tunnel wall effect.

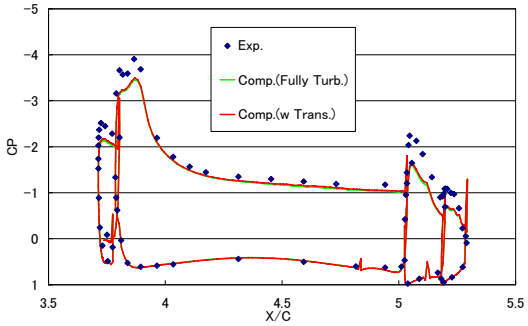

(a) Section B-B

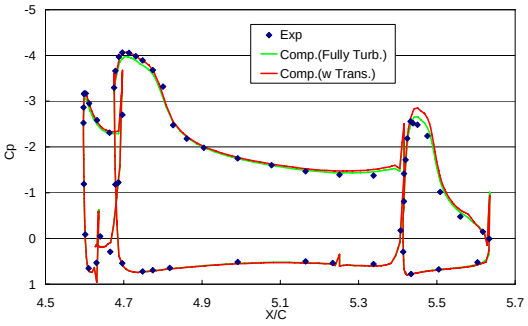

(b) Section E-E

Fig. 7 Comparison of C_p with/without boundary layer transition at α = 10°

Next, capability of a transition prediction method was evaluated to the complex high-lift flows. For high-lift configurations, transitions due to Tollmien-Schlichting (TS) instability, Cross-flow instability (CF) instability, and laminar separation bubbles should be considered. In addition, attachment line contamination and re-laminarisation often occur due to large pressure gradients near the leading-edges of slat, main wing, and flap. Bypass transition due to the wake flow from fore wing element can be an important factor in the flows over multi-element high-lift configurations.

As the prediction code for boundary layer transitions due to TS and CF instability and laminar separation bubbles, LSTAB code [42-44] developed and validated through NEXST-1 (National EXperimental Supersonic Transport) Project in JAXA [45-46] is utilized. LSTAB code utilizes an e^N method based on a linear stability theory of laminar boundary layer. LSTAB code employs a parallel flow approximation to the laminar boundary layer and small disturbance of a plane wave type is assumed. N factor is obtained by an envelope method using integration of amplification rates of each small disturbance. The transition onset is predicted using a threshold of N factor based on a database. In this study, N=4.0 is used for the threshold based on the past experimental results.

For the stability analysis, laminar boundary layer is re-calculated based on the computed C_p using the Kaups & Cebeci method with the conical flow approximation [47]. In the boundary layer computations, laminar separation is detected based on the shape factor, H. In the present method, it is assumed that the transition starts just before the detected location of the laminar separation if the transition due to TS and CF instability does not occur.

For the prediction of attachment line contamination and re-laminarisation, semi-empirical approaches are employed. Attachment line contamination is predicted using the attachment line Reynolds number, $\overline{R}^*$, based on Poll's criterion [48] with an infinite swept cylindrical approximation. Contamination will occur if the value of $\overline{R}^*$ exceeds 245±20.

$$\overline{R}^* \equiv \frac{V_e \eta^*}{\nu^*} = \sqrt{\frac{(V_e)_{s_w=0}^{\ 2}}{\nu^* \left(\frac{dQ_e}{ds_w}\right)_{s_w=0}}} \qquad (1)$$

$$\left(\frac{dQ_e}{ds_w}\right)_{s_w=0} = \frac{2(U_\infty \cos\Lambda)}{r},\ (V_e)_{s_w=0} = U_\infty \sin\Lambda$$

Re-laminarisation is predicted using a parameter, $\overline{K}$, which indicates the acceleration strength of flows [49]. Re-laminarisation will occur if the value of $\overline{K}$ exceeds 5×10^{-6}.

$$\overline{K} = \frac{\nu^*}{Q_e^{\,2}} \frac{dQ_e}{ds_w} \qquad (2)$$

Figure 8 shows the comparisons of transition lines on the upper surface between experimental and predicted results at $\alpha = 10°$. In the figure, the predicted results using measured C_p in the experiment instead of computed C_p in the CFD computations as the input data for the prediction code are also plotted. The transition lines for inner slat are not plotted because the flow kept almost laminar state until the trailing-edge both experimental and predicted results. The transition lines of experimental results for inner main wing are not also plotted because the flow is identified to be turbulent just after the leading-edge.

The transitions on the slats, outer main wing, main flap, are well predicted by the present method although the predicted results on the inner main flap show slightly earlier transitions. For the aft-flap, however, the predicted results using computed C_p show much earlier transitions than the experimental results, while predicted results using measured C_p show good agreement with experimental results. As shown in Fig. 7(a), C_p on the inner flaps shows large difference with the experimental result. In addition, CFD C_p near the leading-edge has a little irregularity related to mesh resolution. It is shown that more consistent C_p obtained in RANS CFD leads to more accurate prediction

For the transition prediction on the inner main wing at $\alpha = 10°$, there is a difference. In the experimental result, the laminar regions are not observed in visible regions, while laminar regions can be observed in the predicted result by CFD C_p. Difference of C_p with experimental results at $\alpha = 10°$ on the section BB shown in Fig. 7(a) may cause the different predictions. In addition, appearance of attachment-line contamination should be also considered especially on the inner main wing.

Figure 9 shows the computational results of $\overline{R}^*$ and $\overline{K}$. For the slat, the computed $\overline{R}^*$ are under the criterion at all span sections. The contamination will not occur on the slat. $\overline{K}$ are over the criterion for re-laminarisation. However, the re-laminarisation will not occur physically because of the absence of attachment line contamination. For the main wing, $\overline{R}^*$ are over the criterion at all spanwise sections, which means that contamination can occur at all spanwise sections. Simultaneously, $\overline{K}$ are over the criterion and re-laminarisation can occur at the all spanwise sections. These results mean that the laminar regions can exist on the inner main wing if the re-laminarisation can occur. On the contrary, the laminar regions are not observed on the inner main wing in the experimental result.

$\overline{K}$ for re-laminarisation parameters computed on the inner main wing are relatively lower than those on the outer main wing and close to the criterion. The acceleration to cause re-laminarisation is not relatively stronger on the inner main wing although the values exceed the criterion. In the present prediction, bypass transition due to the wake flow from fore wing elements is not considered. The three-dimensional vortex in the cove can affect the transition on the leading-edge of the main wing. The possibility due to the bypass transition should be evaluated. Further assessments are now conducted with more detail measurements using hot-films for the transition.

Except for the inner main wing, present approach with several approximations showed reasonable prediction capability.

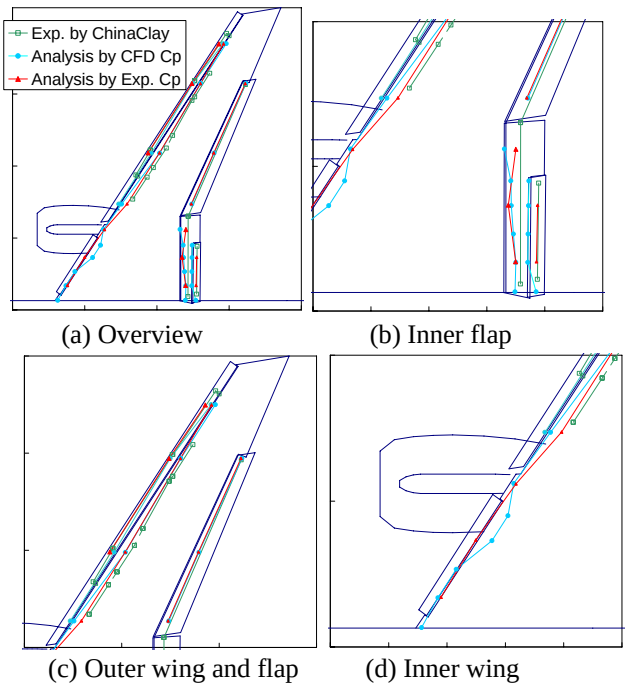

(a) Overview (b) Inner flap

(c) Outer wing and flap (d) Inner wing

Fig. 8 Comparison of transition locations at $\alpha = 10°$.

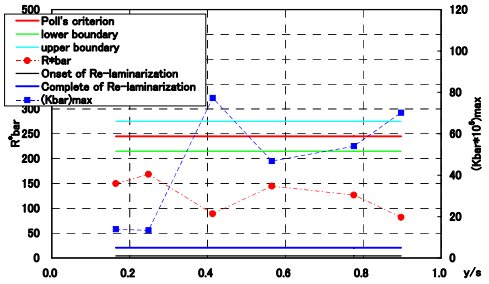

(a) Slat

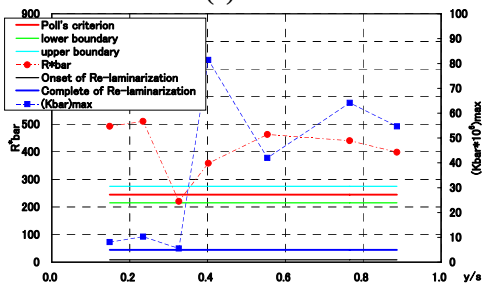

(b) Main wing

Fig. 9 Computed $\overline{R}^*$ and $\overline{K}$ for analysis of attachment line contamination and re-laminarisation at $\alpha = 10°$

4.2 Influence of brackets to support the high-lift devices

The model has eight slat supports, one aft-flap support, and three FTFs. To estimate the influence of brackets to support the high-lift devices, computational results on three configurations; without FTFs and slat and aft-flap supports (Config.1), with FTFs and slat and aft-flap supports (Config2), and without FTFs and with slat and aft-flap supports (Config.3) are compared for the configuration with the long-nacelle. Fully turbulent flow is assumed in the computations.

Figure 10 shows the experimental surface flow patterns at α = 10°. Figure 11 shows the computed surface flow patterns and total pressure distributions at α = 10° on each configuration. The surface flow on the outboard flap for Config.1 shows the flow separation near the flap trailing-edge. In the result of Config.2 with both FTFs and slat supports, the local flow separations also appear on the outboard flap due to the presence of FTFs. Flow separation near the wing tip on the main wing appears in the computation as seen in the experimental results. The oil flow patterns by computations with brackets to support high-lift devices show qualitatively good agreement with experimental results including the local flow separation. The result of Config.3 only with slat supports shows the influences of the wake from slat supports on the main wing. The disturbed wakes by the slat supports cause the local flow separations on the outboard flap.

Figure 12 shows C_L-α and C_M-α. The results of Config.1 and 3 do not show large changes at moderate angles of attack, while the results of Config.2 which has both FTFs and slat supports show larger changes for both C_L and C_M. Lift and nose-down pitching moment are reduced on the Config. 2. The results of oil flow shown in Fig. 11(b) show larger separation on the outboard flap due to the disturbed flow by FTFs. The reduction of the lift on the outboard flap results in the decrease of lift and nose-down pitching moment. The additional supports have possibility to largely affect the flow, especially for the flow separation on the flap and stall performance. For the validation study, the influences of the additional brackets to support high-lift devices also should be well considered.

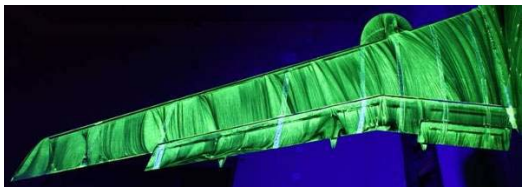

Fig. 10 Measured surface flow pattern at α=10°

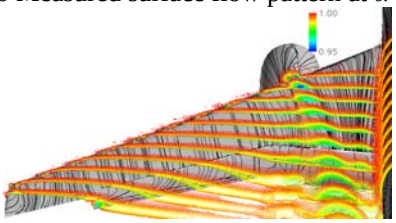

(a) Config.1: w/o FTF w/o Slat Support

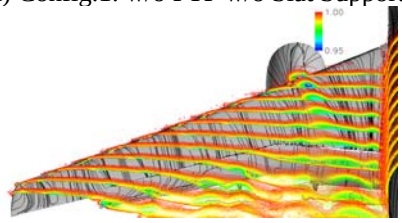

(b) Config.2: w FTF w Slat Support

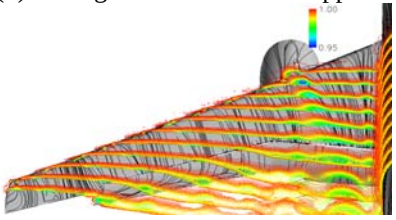

(c) Config.3: w/o FTF w Slat Support

Fig. 11 Computed surface flow pattern and total pressure distributions at α=10°

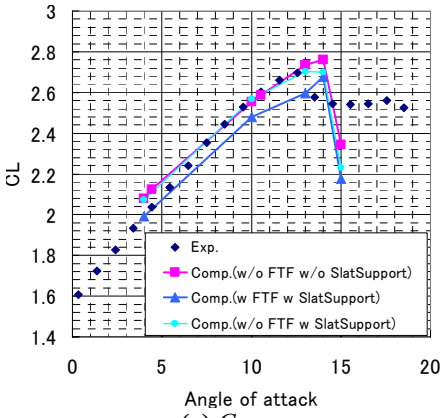

(a) C_L-α

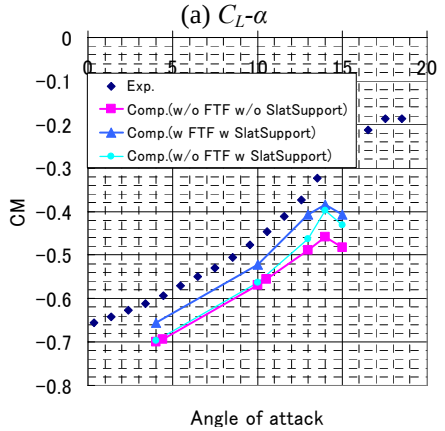

(b) C_M-α

Fig. 12 Variations of aerodynamic forces due to FTFs and slat supports

4.3 Investigation of wind tunnel wall interferences

In the comparison studies between the experimental and numerical results, the wind tunnel wall interferences and the installation effects to the flows and aerodynamic forces have to be well understood. Since the high-lift configurations are tested at large angles of attack and generate large lift, the wind tunnel wall interferences often become large. In addition, the half-span model testing may also include other wall interferences. Here, the wind tunnel wall interferences due to the high-lift half-span model testing are investigated in detail to understand the differences between the flows in the wind tunnel and free-air conditions.

Computations in the free-air conditions and in the wind-tunnel conditions are compared. For the computations of the model in the wind tunnel, the settling chamber, contraction nozzle, and test section as shown in Fig. 13 are included. At the end of the test section, the pressure is recovered with the slot. The exit boundary conditions are enforced at the section.

Figure 14 shows C_L-C_D for the computed results and experimental data. The uncorrected and corrected experimental data after the wind tunnel wall correction are shown. The difference in angle of attack between before and after the correction is about 0.55 degrees at C_{Lmax}.

Drag reductions at constant C_L for the wind tunnel wall interferences are well predicted in the wind-tunnel computations. The deviations from the uncorrected experimental data may come from insufficient grid resolution against the complicated model geometry with high-lift devices in the computations by numerical errors as discussed in Ref. 35. The gradient of C_L-C_D curve is different between the corrected wind tunnel test data and free-air computations. On the other hand, the gradient of C_L-C_D curve of the uncorrected data is well predicted in the wind-tunnel computations.

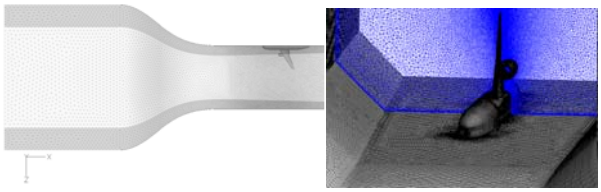

Fig. 13 Computational mesh with the wind tunnel wall

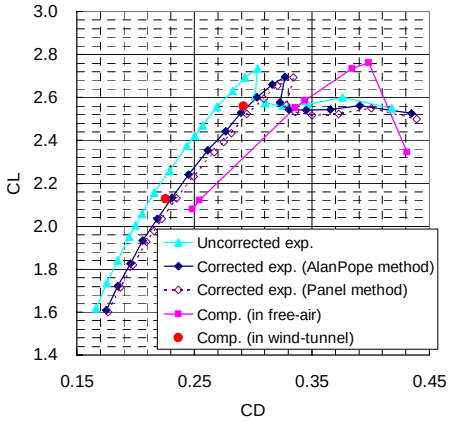

Fig. 14 Comparison of C_L-C_D in free-air and wind-tunnel conditions

Figure 15 shows the comparisons of C_p at the same geometrical α = 10°. Although there are several differences due to the differences of the lift, it is remarkable that the suction peaks on the slat and main wing near the fuselage, which were underpredicted in the free-air computation, show better agreement with experimental results in the wind-tunnel computation. The wind-tunnel computation

shows stronger flow acceleration on the slat and main wing near the fuselage.

Figure 16 shows Mach number contours in the span-wise direction at a span section on the edge of the boundary layer spacer. The boundary layer spacer is expected to work to avoid the boundary layer on the floor of the wind tunnel and minimize the flow in the span-wise direction at the span section to assume the symmetric condition. However, large velocity changes are generated. The positive velocity regions appear near the nose and lower surface of the fore-fuselage. The negative velocity regions appear near the upper surface of the fore-fuselage and lower surface of aft-fuselage. The positive velocity near the lower surface of the fuselage locally increases the velocity and effective angle of attack for the slat and main wings. The local increase of the velocity leads to higher suction peaks of C_p on the slat and main wings in the wind tunnel results.

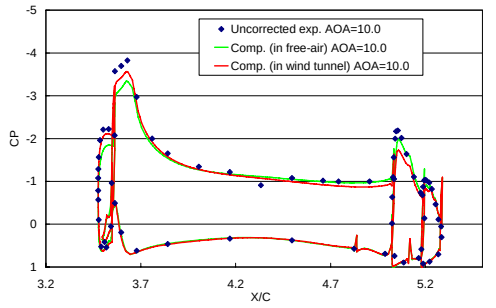

(a) Section A-A

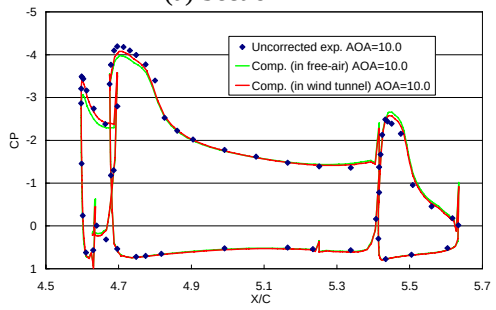

(b) Section E-E

Fig. 15 Comparison of C_p in free-air and wind-tunnel conditions at $\alpha = 10°$

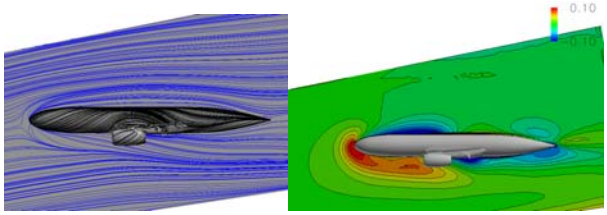

Fig. 16 Oil flow pattern and Mach number contours in the span-wise direction at a span section on the edge of the boundary layer spacer in the wind-tunnel computations

Next, to investigate the influence of the spacer, computations are conducted with the spacer in the free-air conditions excluding the wind-tunnel wall using the computational meshes in Fig.17. In the computations, two kinds of boundary conditions are compared on the bottom floor plane: (1) Slip wall to investigate the influence of the spacer by itself, (2) Non-slip wall to investigate the additional influence of the boundary layer developed on the wind-tunnel floor.

The comparison study is conducted at the heights of the spacer, 30*mm*, 80*mm*, and 160*mm*. Each height is roughly related to the displacement thickness of the boundary layer (+ margin), the stagnation point on the nose of the fuselage (+ margin), and 99% thickness of the boundary layer (+ margin), respectively.

Figure 18 compares C_L-C_D. The forces on the spacer are excluded. With increasing height of the spacer, C_D tends to reduce and C_L tends to increase. The amount of C_D reduction increases with increasing angle of attack and C_L-C_D curve tends to open with the increase of the height. Compared with the results without the floor boundary layer, the computational results with the floor boundary layer show less reduction of C_D and less increment of C_L. The results at the height of 30*mm* agree well with the computations in free-air conditions.

Figure 19 shows the comparisons of C_p on the wing at α = 10°, respectively. With increasing height of the spacer, the results show higher suction peaks for the slat and main elements at inboard section. The computational results with the floor boundary layer show less increment of the suction peaks. Again, the results at the height of 30*mm* agree well with the computations in free-air conditions.

Figure 20 shows the comparison of C_D on each component of the airframe at α = 10°. C_D on the slat, flap, and fuselage decreases with increasing height of the spacer.

Figure 21 shows Mach number contours in the span-wise direction on the edge of the boundary layer spacer. In the computation without the floor boundary layer, the positive velocity component is larger near the nose and lower surface of the fore-fuselage. The negative velocity regions are generated near the lower

surface of aft-fuselage with the floor boundary layer. The result with the floor boundary layer with 160*mm* height spacer shows similar flow pattern with the wind-tunnel computation. These results confirm that the spacer and floor boundary layer generate large positive and negative velocity changes and change the effective angle of attack locally near the fuselage. The positive velocity component generated near the lower surface of the fore-fuselage increases the suction peaks on the slat and mother elements and results in the lift increment and drag reduction on the elements. Increasing velocity change with increasing height of the spacer results in larger change of the forces.

The understanding of the influence by the height and careful selection of the height are important for half-span model tests. A height of the spacer related to the displacement thickness of the floor boundary layer (+margin) showed less difference with the results in the free-air conditions. More detailed discussions on the results are given by Murayama *et al* [16].

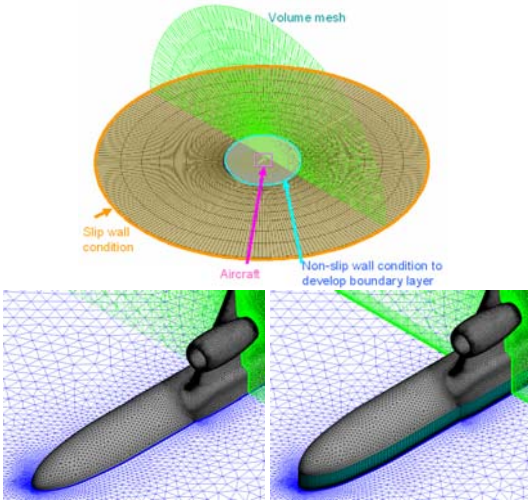

Fig. 17 Computational meshes to conduct parametric study of the height of the spacer

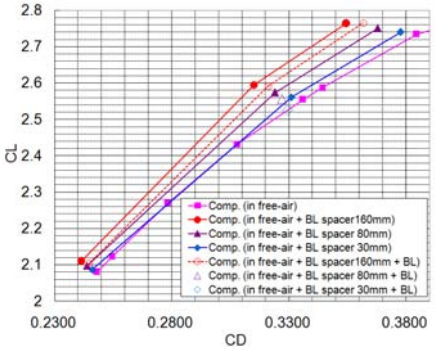

Fig. 18 Comparison of C_L-C_D by the height of boundary layer spacer

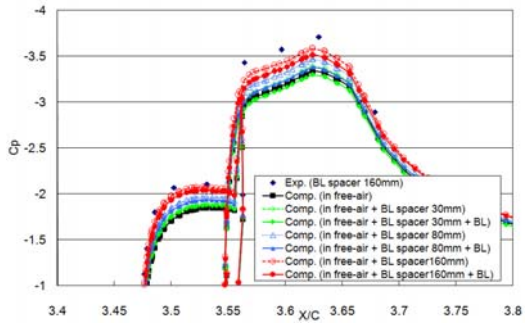

Fig. 19 Comparison of C_p by the height of boundary layer spacer at α = 10°: Close-up view near the slat and main wing at Section A-A

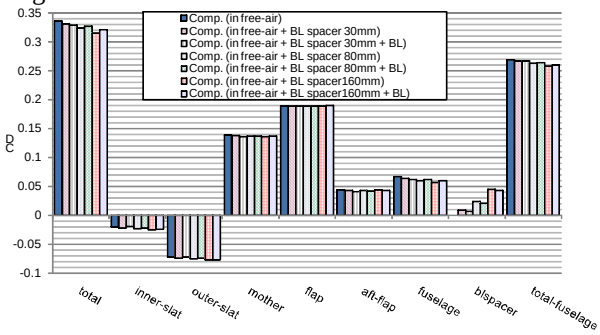

Fig. 20 Comparison of C_L on each component of airframe by the height of boundary layer spacer at α = 10°

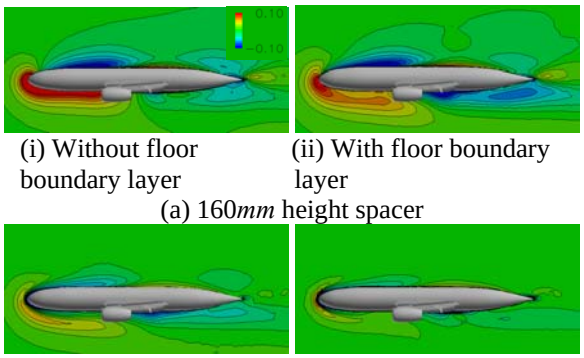

(i) Without floor boundary layer (ii) With floor boundary layer

(a) 160*mm* height spacer

(b) 80*mm* height spacer (c) 30*mm* height spacer

Fig. 21 Mach number contours in the span-wise direction at a span section on the edge of the boundary layer spacer

4.4 Investigation of the interferences between the nacelle-pylon and high-lift devices with nacelle-chine effect

In this section, the results for the improvement of stall performance when deploying high-lift devices by a kind of vortex generator on the nacelle, “nacelle-chine”, are shown. In the wind tunnel tests, the development of efficient design exploration technologies for aerodynamic device installation and investigation of the aerodynamics were conducted in addition to get data for CFD validation. An efficient design process using Kriging response surface method

was used to decide the nacelle-chine installation point. Several reference installation points are evaluated in the wind tunnel and the accuracy of the response surface is efficiently improved by additional evaluation points selected using EI (Expected Improvement) values which consider both possible errors of the response surface and optimality of the objective functions [17-20]. More information of the methodology and consideration of the results in detail are given by Kanazaki *et al* [20].

The test was conducted on a configuration with the short nacelle. Figures 22 and 23 show the design parameters as for the longitudinal and azimuth direction and the obtained response surface for C_{Lmax} at U_∞=60*m/s*. Figure 24 shows C_L-α at six selected locations. The nacelle-chines installed at pointA, pointB, or pointF remarkably improved C_{Lmax}. The efficient and reliable response surface method is effective not only to decide an optimum location but also to consider the robustness of the installation.

The vortex behaviors for three installation locations at pointA, pointB, and pointF were investigated by PIV in detail. Figure 25 shows the contours of velocity magnitude at U_∞ = 60*m/s* and α = 16°. In Fig. 25(a) without the chine, the separated and disturbed flow from the pylon regions are clearly observed on the upper surface of the main wing, which cause the lift reduction. In the case with the chine at pointF shown in Fig. 25(b), the other vortex with the same rotating direction generated by the chine appears crossing on the original vortex. This vortex reduces the separated and disturbed flow from the nacelle-pylon. In the cases at pointB and PointA, similar improvement of C_{Lmax} can be obtained but the interaction of the vortices are different as shown in Fig.25(c) and (d). More discussions on the results are given by Kato *et al* [21] and Yokokawa *et al* [22].

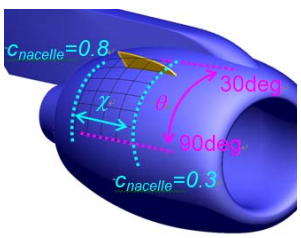

Fig. 22 Design space for the chine installation

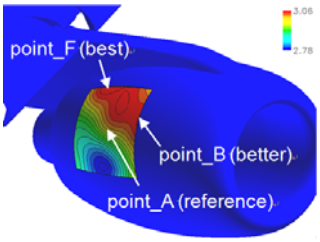

Fig. 23 Resulting response surface of C_{Lmax}

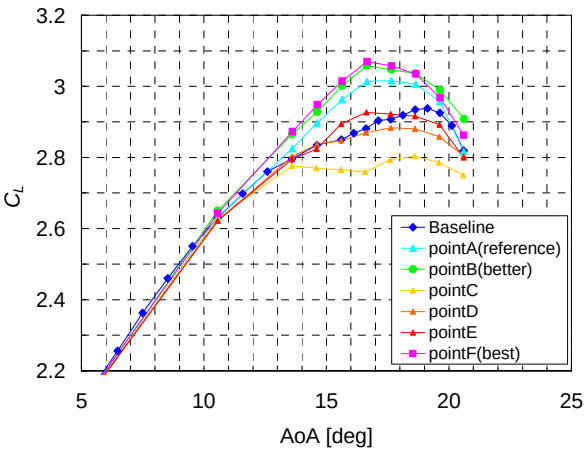

Fig. 24 Effects of the nacelle-chine installation

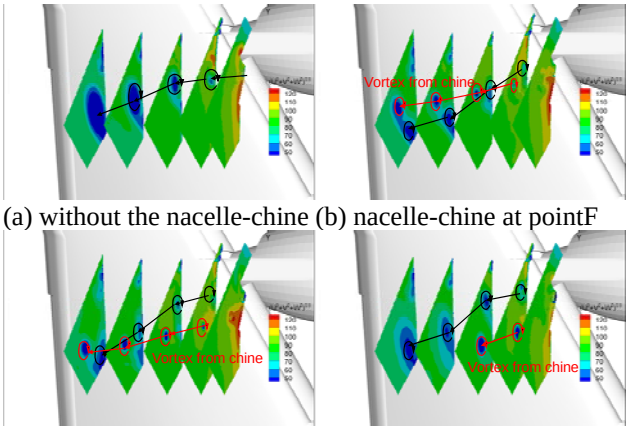

(a) without the nacelle-chine (b) nacelle-chine at pointF

(c) nacelle-chine at pointB (d) nacelle-chine at pointA

Fig. 25 Comparison of velocity magnitude measured by PIV

For CFD simulations with changed position of small devices such as nacelle-chine, it takes time to create each high-quality volume mesh using stretched or anisotropic elements for viscous flow simulations. University of Alabama at Birmingham (UAB) has developed an efficient and automatic local remeshing method for hybrid mesh [33] with JAXA. Figures 26 and 27 show the local remeshing process and resulting mesh for a nacelle-chine. The intersections are trimmed and the surface and volume mesh is remeshed in the detected remeshing regions. Figure 28 shows the computational results with changed position of a nacelle-chine. Besides the time saving on the mesh generation, converged solutions can be obtained mush faster due to the restart from the computational result on the baseline mesh. The flow simulation is conducted with a solution-adaptive mesh refinement technique if needed.

In Fig. 29, the computational results are compared with PIV results. Although it is still difficult to simulate the flow fields quantitatively as for this kind of separated flows and vortex interactions on the complete high-lift aircraft configurations, the vortex behaviors are well simulated and the results are helpful to know efficient control mechanism of the separated flow. Additional mesh generation method to resolve the wake vortices efficiently is our future work to improve the accuracy of the prediction.

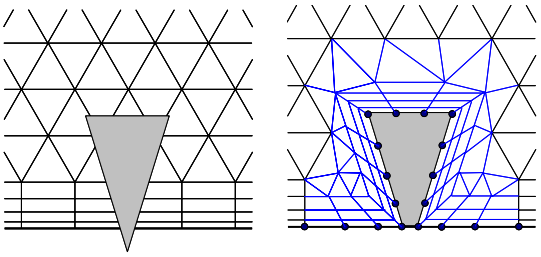

(a) (b)

Fig. 26 Local remeshing process: (a) a baseline hybrid mesh and a new geometry added; (b) remeshing on the trimmed boundary surface and in the remeshing region

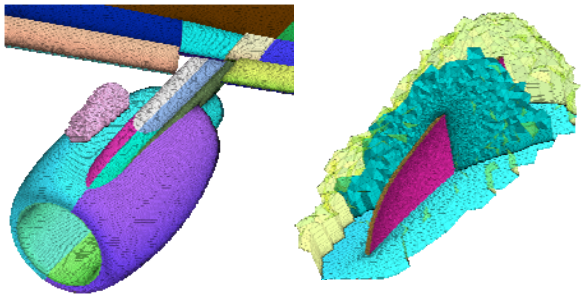

Fig. 27 Local remeshing region and resulting mesh for installation of a nacelle-chine

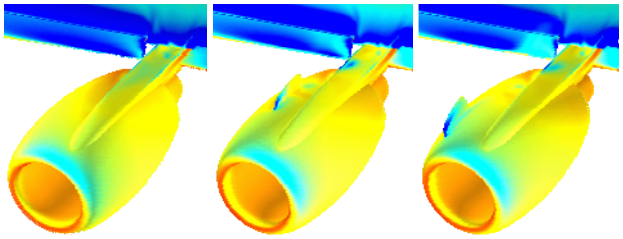

(a) w/o chine (b) Position F (c) Position B

Fig. 28 Computational results with change of a nacelle-chine location using local remeshing method

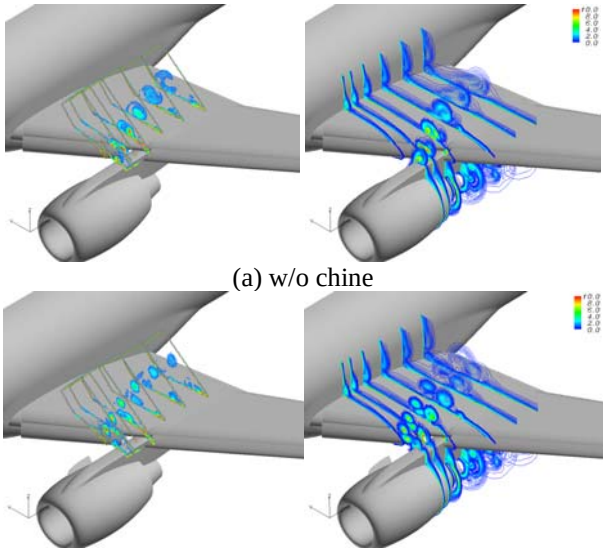

(a) w/o chine

(b) Position F

Fig. 29 Comparison of vorticity magnitude by PIV and CFD (left: PIV, right: CFD)

4.5 Investigation of setting effect of high-lift devices and its CFD prediction

In the wind tunnel tests, several setting effects of high-lift devices were evaluated for validation of CFD and aerodynamic design optimization methods [17-19]. In addition, comparisons of several different configurations were conducted such as configurations with a short-type or long-type nacelle, configurations with/without the nacelle-pylon, configurations with/without the inboard slat cut-off between the fuselage and inboard slat, and so on as shown in Fig. 2. For practical use, it is important to predict the aerodynamic change due to the setting difference and geometrical difference within a reasonable accuracy.

Figure 30 shows the comparison of C_L-α at moderate and high flap deflection angles (δ_F) of 30° and 35° on a configuration with a short-type nacelle. Figures 31 and 32 show the comparison of the surface oil-flow at α = 10°. The experimental result at δ_F = 35° shows C_L increment by 0.1 at moderate angles of attack. On the other hand, the flow separation near the trailing-edge on the flap appears more largely at δ_F = 35° as shown in Fig. 31.

The computational results were obtained on a coarse (6~7M mesh points) mesh without FTF and slat supports. The computational result shows the C_L increment at δ_F = 35°. However,

the expected amount of C_L increment is not sufficiently obtained because the flow separation on the flap is much larger in the computation as shown in Fig. 32. Other studies show the size of the flow separation on the flap depends on the mesh density and turbulence models. The prediction of the flow at high deflection angle within a good accuracy is still difficult case with large flow separation on the flap. It is engineeringly important to known the limitation of the deflection angle and further efforts are required to predict the effect.

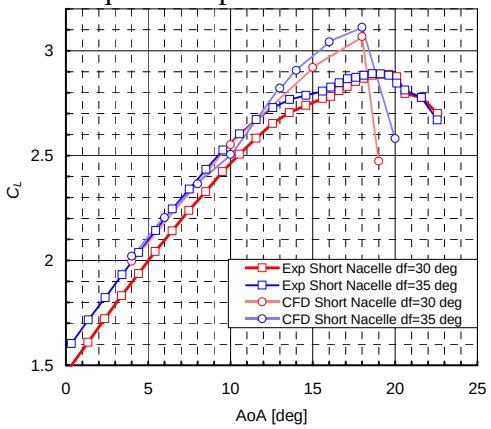

Fig. 30 Comparison of C_L-α by flap deflection angle, δ_F

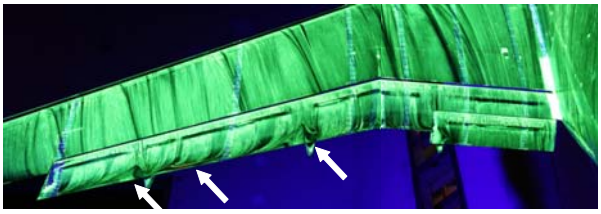

(a) δ_F = 30°

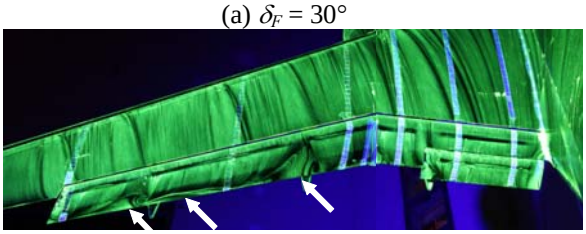

(b) δ_F = 35°

Fig. 31 Comparison of measured surface flow pattern at α = 10° by flap deflection angle, δ_F

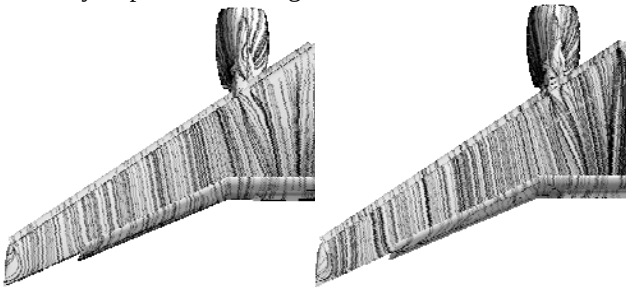

(a) δ_F = 30° (b) δ_F = 35°

Fig. 32 Comparison of computed surface flow pattern at α = 10° by flap deflection angle, δ_F

5 Conclusion

Several aerodynamic computational studies related to a series of wind tunnel tests using a realistic civil aircraft high-lift model to develop design technologies for advanced high-lift devices have been presented.

The capability and applicability of a transition prediction method combined with RANS CFD using an e^N method and semi-empirical methods has been validated to the complex high-lift flows. It was shown that the present method can predict the transition locations in a reasonable accuracy and more consistent *Cp* obtained in RANS CFD leads to more accurate prediction although further assessments will be required with more detail measurements as for the bypass transition, attachment line contamination, and re-laminarisation.

The influence of brackets to support the high-lift devices has been also discussed. The disturbed wakes by the slat brackets had a large interference not only on the main wing but also on the flap. The additional supports have possibility to largely affect the flow, especially for stall performance. The influences should be well considered for the validation study.

CFD investigation of wind tunnel wall interferences using half-span testing model showed the influence of the boundary layer spacer to the flow and the best height of the spacer. With increasing height of the boundary layer spacer, the spacer and floor boundary layer generate larger positive and negative velocity changes in the plane to assume the symmetric condition and change the effective angle of attack locally near the fuselage. It results in increment of suction peaks of C_p on the slat and mother elements at inboard sections and reduction of C_D. The amount of the change increases with increasing angle of attack and it can cause C_L-C_D curve difference. Through the investigations, a height of the spacer related to the displacement thickness of the floor boundary layer (+margin) showed less difference with the results in the free-air conditions.

Some of investigations on the interferences between the nacelle-pylon and high-lift devices

with nacelle-chine effect and setting effect of high-lift devices and their CFD predictions have been also shown. In the cases with largely separated flow and vortex interactions, the effects could be predicted within a reasonable accuracy but the accuracy is not necessarily enough. It is still difficult to simulate the flow fields quantitatively as for these kinds of separated flows and vortex interactions on the complete high-lift aircraft configurations. On the other hand, it is engineeringly important to predict the three-dimensional flow interactions between the nacelle-pylon and the high-lift devices, the limitation of the flap deflection angle, and so on. In addition to improvement of stall prediction, further efforts are required to predict such effects more accurately with more studies on the mesh density, turbulence model, and additional mesh generation method to resolve the wake vortices efficiently.

Acknowledgement

We would like to express our gratitude and appreciation to members of Lowspeed Wind Tunnel Section in JAXA, for their generous support and large amount of efforts throughout the experiment. Great thanks must also be addressed to Mr. Tanaka, Mr. Hirai, Mr. Ueda, Mr. Uchida, Dr. Amemiya, Mr. Ura, Dr. Mitsuo, Mr. Watanabe, and members of Civil Transport Team and Advance Test Section in JAXA, for their specialized and technical support for the whole of this research program.

References

[1] C. P. van Dam, “The aerodynamic design of multi-element high-lift systems for Transport Airplanes,” *Progress in Aerospace Science*, Vol.38, 2002, pp. 101-144.

[2] Meredith, P. T., “Viscous Phenomena Affecting High-Lift Systems and Suggestions for Future CFD Development,” *High-Lift Systems Aerodynamics*, AGARD CP 315, Sep. 1993, pp. 19-1 – 19-8.

[3] Hansen, H., Thiede, P., Moens, F., Rudnik, R., and Quest, J., “Overview about the European High Lift Research Programme EUROLIFT,” AIAA Paper 2004-0767, Jan. 2004.

[4] Rudnik, R. and Germain, E., “Re-No. Scaling Effects on the EUROLIFT High Lift Configurations,” AIAA Paper 2007-0752, Jan. 2007.

[5] Rudnik, R., Geyr, H., Frhr, v., “The European High Lift Project EUROLIFT II – Objectives, Approach, and Structure,” AIAA Paper 2007-4296, June 2007.

[6] Lei, Z., Murayama, M., Takenaka, K., and Yamamoto, K., “CFD Validation for High-Lift Devices: Two-Element Airfoil,” *Transactions of the Japan Society for Aeronautical and Space Sciences*, Vol. 49, No. 163, May 2006, pp. 31-39.

[7] Murayama, M., Lei, Z., Mukai, J., and Yamamoto, K., “CFD Validation for High-Lift Devices: Three-Element Airfoil,” *Transactions of the Japan Society for Aeronautical and Space Sciences*, Vol. 49, No. 163, May 2006, pp. 40-48.

[8] Murayama, M., Yamamoto, K., and Kobayashi, K., “Validation of Computations Around High-Lift Configurations by Structured- and Unstructured-Mesh,” *Journal of Aircraft*, Vol. 43, No.2 , March-April 2006, pp. 395-406.

[9] Murayama, M., Imamura, T., Yamamoto, K., and Kobayashi, K., “Comparison of Reynolds-Averaged Navier-Stokes Simulations of Multi-Element High-Lift Configurations,” *Journal of Aircraft*, Vol. 44, No. 1, 2007, pp. 175-186.

[10] Ito, T., Ura, H., Yokokawa, Y., Kato, H., Mitsuo, K., and Yamamoto, K., “High-Lift Device Testing in JAXA 6.5m×5.5m Low-speed Wind Tunnel,” AIAA Paper 2006-3643, June 2006.

[11] Yokokawa, Y., Murayama, M., Ito, T., and Yamamoto, K., “Experimental and CFD of a High-Lift Configuration Civil Transport Aircraft Model,” AIAA Paper 2006-3452, June 2006.

[12] Mitsuo, K., Kurita, M., Kuchi-Ishi, S., Fujii, K., Ito, T., and Watanabe, S., “PSP Measurement of a High-Lift Device Model in JAXA 6.5m×5.5m Low-speed Wind Tunnel,” AIAA Paper 2007-1065, Jan. 2007.

[13] Kato, H., Watanabe, S., Hashimoto, T., Fujii, K., Ito, T., and Yamamoto, K., “PIV Measurement of a High-Lift Device Model in JAXA 6.5m×5.5m Low-speed Wind Tunnel,” AIAA Paper 2007-1064, Jan. 2007.

[14] Yokokawa, Y., Murayama, M., Kanazaki, M., Murota K., Ito, T., and Yamamoto, K, “Investigation and Improvement of High-lift Aerodynamic Performances in Lowspeed Wind Tunnel Testing,” AIAA Paper 2008-350, Jan. 2007.

[15] Murayama, M., Yokokawa, Y., Yamamoto, K., and Ueda, Y., “CFD Validation Study for a High-Lift Configuration of a Civil Aircraft Model”, AIAA Paper 2007-3924, June 2007.

[16] Murayama, M., Yokokawa, Y., Tanaka, K., Yamamoto, K., and Ito, T., “Numerical Simulation of Half-span Aircraft Model with High-Lift Devices in Wind Tunnel,” AIAA Paper 2008-0333, Jan. 2008.

[17] Jeong, S., Murayama, M., and Yamamoto, K., “Efficient Optimization Design Method Using Kriging Model,” *Journal of Aircraft*, Vol. 42, No. 2, 2005, pp. 413-420.

[18] Kanazaki, M., Tanaka, K., Jeong., S., and Yamamoto, K., "Multi-Objective Aerodynamic Exploration of Elements' Setting for High-Lift Airfoil Using Kriging Model," *Journal of Aircraft*, Vol. 44, No. 3, 2007, pp. 858-864.

[19] Kanazaki, M., Imamura, T., Jeong., S., and Yamamoto, K., "High-Lift Wing Design in Consideration of Sweep Angle Effect Using Kriging Model," AIAA Paper 2008-175, Jan. 2008.

[20] Kanazaki, M., Yokokawa, Y., Murayama, M., Ito, T., Jeong, S., and Yamamoto, K., "Efficient Design Exploration of Nacelle Chine Installation in Wind Tunnel Testing," AIAA Paper 2008-155, Jan. 2008.

[21] Kato, H., Watanabe, S., Murayama, M., Yokokawa, Y., and Ito, T., "PIV Investigation of Nacelle Chine Effects on High-Lift System Performance," AIAA paper 2008-240, Jan. 2008.

[22] Yokokawa, Y., Kanazaki, M., Murayama, M., Kato, H., Ito, T., and Yamamoto, K., "Investigation of the Flow over Nacelle/Pylon and Wing Controlled with a Vortex Generator in High-Lift Configuration," *Proceedings of 26th ICAS*, 2008.

[23] Ura, H., Yokokawa, Y., and Ito, T., "Phased Array Measurement of High Lift Devices in Low Speed Wind Tunnel," AIAA Paper 2006-2565, May 2006.

[24] Imamura, T., Enomoto, S., Yokokawa, Y., and Yamamoto, K., "Three-Dimensional Unsteady Flow Computations Around a Conventional Slat of High-Lift Devices," *AIAA Journal*, Vol. 46, No. 5, 2008, pp. 1045-1053.

[25] Ura, H., Yokokawa, Y., Imamura, T., Ito, T., and Yamamoto, K., "Investigation of Airframe Noise from High Lift Configuration Model," AIAA Paper 2008-019, Jan. 2008.

[26] Imamura, T., Ura, H., Yokokawa, Y., Hirai, T., Yamamoto, K., "Numerical and Experimental Research of Low-Noise Slat Using Simplified High-Lift Model," AIAA Paper 2008-2918, May 2008.

[27] Yokokawa, Y., Imamura, T., Ura, H., Uchida, H., Ito, T., and Yamamoto, K., "Studies on Airframe Noise Generation at High-lift Devices in Relation to Aerodynamic Performances," AIAA Paper 2008-2960, May 2008.

[28] Toyoda, A., Misaka, T., and Obayashi, S., "An Application of Local Correlation-Based Transition Model to JAXA High-Lift Configuration Model," AIAA Paper 2007-4286, June 2007.

[29] Nakayama, R., Matsushima, K., and Nakahashi, K., "CFD Validation about High-Lift Configuration of Civil Transport Aircraft", AIAA Paper 2008-0410, Jan. 2008.

[30] Ito, Y. and Nakahashi, K., "Surface Triangulation for Polygonal Models Based on CAD Data," *International Journal for Numerical Methods in Fluids*, Vol. 39, Issue 1, 2002, pp. 75-96.

[31] Sharov, D. and Nakahashi, K., "A Boundary Recovery Algorithm for Delaunay Tetrahedral Meshing," *Proceedings of 5th International Conference on Numerical Grid Generation in Computational Field Simulations*, Mississippi State, Mississippi, 1996, pp. 229-238.

[32] Ito, Y. and Nakahashi, K., "Improvements in the Reliability and Quality of Unstructured Hybrid Mesh Generation," *International Journal for Numerical Methods in Fluids*, Vol. 45, Issue 1, May 2004, pp. 79-108.

[33] Ito, Y., Murayama, M., Yamamoto, K., Shih, A. M., and Soni, B. K., "Efficient CFD Evaluation of Small Device Locations with Automatic Local Remeshing," AIAA Paper 2008-7180, August 2008.

[34] Nakahashi, K., Togashi, F., Fujita, T., and Ito, Y., "Numerical Simulations on Separation of Scaled Supersonic Experimental Airplane from Rocket Booster at Supersonic Speed," AIAA Paper 2002-2843, June 2002.

[35] Murayama, M. and Yamamoto, K., "Comparison Study of Drag Prediction for the 3rd CFD Drag Prediction Workshop by Structured and Unstructured Mesh Method," AIAA Paper 2007-0258, Jan. 2007.

[36] Obayashi, S. and Guruswamy, G. P., "Convergence Acceleration of an Aeroelastic Navier-Stokes Solver," *AIAA Journal*, Vol. 33, No. 6, 1995, pp. 1134-1141.

[37] Burg, C., "Higher Order Variable Extrapolation For Unstructured Finite Volume RANS Flow Solvers," AIAA Paper 2005-4999, 2005.

[38] Sharov, D. and Nakahashi, K., "Reordering of Hybrid Unstructured Grids for Lower-Upper Symmetric Gauss-Seidel Computations," *AIAA Journal*, Vol. 36, No. 3, 1998, pp. 484-486.

[39] Spalart, P. R. and Allmaras, S. R., "A One-Equation Turbulence Model for Aerodynamic Flows," AIAA Paper 92-0439, Jan. 1992.

[40] Lei, Z., "Effect of RANS Turbulence Models on Computational of Separated Flows over a Wing-Body Configuration," *Transactions of the Japan Society for Aeronautical and Space Sciences*, Vol. 48, Nov. 2005, pp. 150-160.

[41] Matsuo, Y., Nakamura, T., Tsuchiya, M., Ishizuka, T., Fujita, N., Ohkawa, H., Hirabayashi, Y., Takaki, R., Yoshida, M., Nakamura, K., Yamamoto, K., Suematsu, K., and Iwamiya, T., "Numerical Simulator III – Building a Terascale Distributed Parallel Computing Environment for Aerospace Science and Engineering," *Proceedings of the Parallel CFD 2002 Conference*, Nara, Japan, Elsevier Science B. V., 2003, pp. 187-194.

[42] Yoshida, K., Ogoshi, H., Ishida, Y., and Noguchi, M., "Numerical Study on Transition Prediction Method and Experimental Study on Effect of Supersonic Laminar Flow Control," NAL-SP 31, 1996, pp. 59-79.

[43] Yoshida, K., Ishida, Y., Noguchi, M., Ogoshi, H., and Inagaki, K., "Experimental and Numerical Analysis of Laminar Flow Control at Mach 1.4," AIAA Paper 99-3655, 1999.

[44] Ueda, Y., Ishikawa, H., and Yoshida, K., "Three Dimensional Boundary Layer Transition Analysis in Supersonic Flow Using A Navier-Stokes Code," ICAS 2004-2.8.2, 2004.

[45] wamiya, T., "A Computational Study on Unmanned Scaled Supersonic Experimental Airplane," AIAA Paper 2002-2841, 2002.

[46] Yoshida, K., Makino, Y., and Shimbo, Y., "An Experimental Study on Unmanned Scaled Supersonic Experimental Airplane," AIAA Paper 2002-2842, 2002.

[47] Kaups, K. and Cebeci, T., "Compressible Laminar Boundary Layers with Suction on Swept and Tapered Wings," *Journal of Aircraft*, Vol. 14, No. 7, July 1977, pp. 661-667.

[48] Poll, D. I. A., "Some Aspects of the Flow Near a Swept Attachment Line with Particular Reference to Boundary Layer Transition," Cranfield Inst. of Technology, CoA Rept. 7805, August 1978.

[49] Beasley, J. A., "Calculation of the Laminar Boundary Layer and Prediction of Transition on a Sheared Wing," Royal Aeronautical Establishment, Rept. 3787, October 1973.

Copyright Statement